Computers & Fluids 39 (2010) 1696–1703

Contents lists available at ScienceDirect

Computers & Fluids

journal homepage: www.elsevier.com/locate/compfluid

Droplet impingement and breakup on a dry surface

Amit Gupta, Ranganathan Kumar *

Department of Mechanical, Materials and Aerospace Engineering, University of Central Florida, Orlando, FL 32816, USA

ARTICLE INFO

Article history:
Received 25 February 2009
Received in revised form 15 March 2010
Accepted 5 June 2010
Available online 15 June 2010

Keywords:
Lattice Boltzmann
Droplet
Impingement
Spread factor

ABSTRACT

In this work, new results of droplet impingement and breakup have been obtained using three-dimensional lattice Boltzmann method. All four phases after impingement, the kinematic, spreading, relaxation and equilibrium phases, leading to breakup have been obtained for a range of Weber number, Reynolds number and density ratio. Conditions have been chosen such that $\sqrt{\mathrm{Re}} \ll \mathrm{We}$ for comparison with available data in the literature. The maximum spread factor compares well with experiments as well as the theoretical value of 0.5 $\mathrm{Re}^{0.25}$. At Oh < 0.15 and Capillary number, Ca < 1.0, the relaxation phase is marked by the presence of strong oscillations in the spreading diameter. An analytical solution for breakup based on the conservation of energy is provided. Criteria for three-dimensional droplet breakup have been developed as functions of Re and We.

1. Introduction

Collision of droplet(s) on solid or liquid surfaces is a phenomenon that occurs widely in nature. Droplet impact dynamics is an area which has long been an area of interest. Impact of drops on solid surfaces is a very common phenomenon in many modern engineering applications ranging from ink-jet printing to spray cooling, internal combustion engines to spray painting and plasma spraying, and more recently in microfabrication and microchannels [1]. In high pressure applications such as in nuclear reactors, the liquid to vapor density ratio is less than 10 at 2.4 MPa. When these liquid droplets hit a solid surface, the accompanying physical behavior is observed to be very different, depending upon whether the surface is hydrophobic or hydrophilic, rough or smooth and whether it is dry or wet. The final shape and spreading of the liquid drop also depends on a range of parameters, like the impact velocity, the size of the droplet, the angle of attack to the surface, the physical properties of the liquid drop and the surrounding pressure.

Experimental investigations have been carried out extensively to study the mechanism of droplet impact and the subsequent spreading process on a dry surface [2–4]. These studies show the formation of a watersheet as well as the subsequent breakup into daughter droplets. The difference in the dynamics of a single drop impact with a dry wall as compared to that of a train of drops has been demonstrated as well [4]. In a detailed experimental study [5], it was shown that for the case of water drops impacting a wax surface, the perturbations during the receding process merge continuously leading to a rebound of the droplet from the surface. For the case where there is no rebound of the liquid film from the surface, the spreading diameter may stay constant or increase depending upon the wettability of the surface used. In a separate study [6], it was shown that the maximum spread factor follows the correlation given by $\xi_{max} = 0.61(\mathrm{Re}^2\mathrm{Oh})^{0.166}$, and that the contact angle effect on the spreading diameter is negligible for droplet Re > 10.

Simulations of droplet splashing phenomenon have mostly focused on impact dynamics on a wet surface with a thin liquid film [7,8], deposition/splashing behavior of impact of single drop on a wet surface [9–11] and the study of droplet spreading behavior for very low Oh and subsequent rebound on a dry surface for low density ratios [12]. However, an analytical investigation of the droplet spreading behavior in high pressure systems at early times of impact to droplet breakup has not been carried out so far. The objective of this work is to (1) develop a three-dimensional LBM simulation to quantify the spreading film radius for various Re and We, (2) compare these low density ratio results with known experimental data, (3) analytically quantify the criterion that would result in breakup of the droplet upon impact on a dry surface.

2. Lattice Boltzmann model

In recent years, LBM has emerged as a powerful tool to study two-phase fluid flow interfaces in two-phase flows and porous media. LBM offers significant advantages over conventional CFD solvers due to its local nature of interactions, and a simple collision-streaming process that does not require any time consuming iterations. In addition, the interface separating the liquid and vapor

* Corresponding author. Tel.: +1 407 823 4389; fax: +1 407 823 0208.
E-mail address: Rnkumar@mail.ucf.edu (R. Kumar).

0045-7930/$ - see front matter © 2010 Elsevier Ltd. All rights reserved.
doi:10.1016/j.compfluid.2010.06.006

Nomenclature

a	acceleration
a	index for velocity-space discretization
b	number of lattice directions
c	lattice unit length
c_s	speed of sound
Ca	Capillary number, $\mu U/\sigma$ = We/Re
d	diameter of the spreading film
D	diameter of the spherical drop
$\mathbf{e}_i$	lattice speed of particles moving in direction i
f	particle distribution function
F	force
g	acceleration due to gravity
g	fluid–fluid interaction strength
G	Green's function
m	molecular mass
N	number of links at each lattice point
Oh	Ohnesorge number = $\mu/(\rho\sigma D)^{1/2}$ = $We^{1/2}$/Re
p	pressure
p	momentum
r	radius of the drop
Re	Reynolds number = $\rho_l UD/\mu$
s	curvature of the stagnation point
S	number of phases
t	time
u	velocity
U	velocity in the fall direction
V	interaction potential
We	Weber number = $\rho_l U^2 D/\sigma$

Greek symbols

ρ	density
σ	surface tension
μ	dynamic viscosity
ν	kinematic viscosity
τ	relaxation time
ξ	spread factor
Ω	collision operator
θ	contact angle
$\delta_{\alpha\beta}$	Kronecker delta
Ψ	effective mass function
Φ	dissipation function

Subscripts

crit	critical
e	effective
ext	external
i	index
int	interaction
g	gas
l	liquid
sph	sphere
tot	total
w	wall
σ	phase index

Superscripts

$*$	non-dimensional quantities
eq	equilibrium
σ	phase index

evolves on its own as a result of the zeroth-order closure of the distribution function, and does not need to be tracked or constructed as is the case with Marker-cell or Volume-of-fluid methods. LBM requires no empirical correlations for closure of the extra source terms in the governing equations as the microscopic nature of interactions between fluid particles is monitored using the distribution function. As a result, no closure terms are needed, as opposed to conducting a similar multiphase simulation using CFD, to approximate the nature of forces between dissimilar fluids. Thus, LBM can yield detailed information about the physics of the flow around single or multiple droplets. The interface is no longer a mathematical boundary; rather it is a post-processed quantity that can be detected by monitoring the variation in fluid densities.

The Boltzmann's kinetic equation describes the evolution of the single particle distribution function. Unlike conventional schemes that are based on discretization of continuum based macroscopic equations, the lattice Boltzmann method models the kinetic equations. The fundamental idea of LBM is to construct simplified kinetic models that incorporate the essential physics of microscopic processes so that the macroscopic averaged properties obey the desired macroscopic equations.

The evolution equation for the particle distribution function is very similar to the kinetic equation in lattice gas automata, given by

$$f_i(\mathbf{x}+\mathbf{e}_i\delta t, t+\delta t) = f_i(\mathbf{x},t) + \Omega_i(f_i(\mathbf{x},t)), \quad i = 0,1,\ldots,N$$

and

$$\Omega_i(f_i(\mathbf{x},t)) = -\frac{f_i(\mathbf{x},t) - f_i^{eq}(\mathbf{x},t)}{\tau} \tag{1}$$

In this work, the well known three-dimensional, nineteen speed phase-space discretization model, D3Q19, for the discrete velocity space has been used that gives a cubic lattice for the space discretization.

We have used the particular form of the collision operator with the single time relaxation approximation, also known as the lattice Bhatnagar–Gross–Krook (BGK) operator. This form of the collision operator leads to a differential equation of the form

$$\frac{\partial f_i}{\partial t} + \mathbf{e}_i \cdot \nabla f_i = -\frac{(f_i - f_i^{eq})}{\tau} \tag{2}$$

for the Boltzmann's kinetic equation. In the low frequency, long wavelength limit, the Chapman–Enskog expansion can be used under the assumption that $\delta x \approx \delta t \approx \varepsilon$, where ε is a small parameter as compared to the macroscopic scales. Thus,

$$f_i = f_i^{eq} + \varepsilon f_i^{(1)} + \varepsilon^2 f_i^{(2)} + O(\varepsilon^3) \tag{3a}$$

$$\frac{\partial}{\partial t} = \varepsilon\frac{\partial}{\partial t_1} + \varepsilon^2\frac{\partial}{\partial t_2}, \quad \frac{\partial}{\partial x} = \varepsilon\frac{\partial}{\partial x_1} \tag{3b}$$

Substituting in Eq. (1) and filtering out $O(\varepsilon^0)$ and $O(\varepsilon^1)$ terms leads to

$$\frac{\partial f_i^{eq}}{\partial t_1} + \mathbf{e}_i \cdot \nabla_1 f_i^{eq} = -\frac{1}{\tau} f_i^{(1)} \tag{4a}$$

and

$$\frac{\partial f_i^{eq}}{\partial t_2} + \left(1 - \frac{1}{2\tau}\right)\left(\frac{\partial f_i^{(1)}}{\partial t_1} + \mathbf{e}_i \cdot \nabla_1 f_i^{(1)}\right) = -\frac{1}{\tau} f_i^{(2)} \tag{4b}$$

The macroscopic density per node and the macroscopic momentum density are defined in terms of the particle distribution functions by

$$\rho = \sum_i f_i = \sum_i f_i^{eq} \; ; \quad \rho \mathbf{u} = \sum_i f_i \mathbf{e}_i = \sum_i f_i^{eq} \mathbf{e}_i \tag{5}$$

The equilibrium distribution functions depend only on local density and velocity and they can be expressed in the following form

$$f_i^{eq} = \begin{cases} \frac{1}{3}\rho(1 - \frac{3}{2}\mathbf{u}\cdot\mathbf{u}), & i = 0 \\ \frac{1}{18}\rho(1 + 3\mathbf{e}_i\cdot\mathbf{u} + \frac{9}{2}(\mathbf{e}_i\mathbf{u})^2 - \frac{3}{2}\mathbf{u}\cdot\mathbf{u}), & i = 1,\ldots,6 \\ \frac{1}{36}\rho(1 + 3\mathbf{e}_i\cdot\mathbf{u} + \frac{9}{2}(\mathbf{e}_i\mathbf{u})^2 - \frac{3}{2}\mathbf{u}\cdot\mathbf{u}), & i = 7,\ldots,18 \end{cases} \tag{6}$$

where f_i^{eq} is the equilibrium distribution of particles moving in direction '*i*', f_0^{eq} is the equilibrium distribution of rest particles [13]. This form of the equilibrium distribution function can be simplified to the macroscopic governing equation. Thus the lattice Boltzmann's equation is able to bridge the gap between microscopic and macroscopic fluid interactions as it yields the Navier–Stokes equation in the low Mach number limit using the Chapman–Enskog expansion, and is second order accurate in space. The limitation in the current simulations is due to relaxation time and not the time step or lattice spacing. The Shan–Chen model, together with the BGK operator, was found to be stable for density ratios different from 1 for relaxation time (τ) equal to 1. In addition, $\tau > 1/2$ in order for viscosity to be positive.

2.1. Multiphase model in LBM

A few methods have been proposed over the past decade to conduct multiphase simulations using LBM [14,15,17–20]. In the chromodynamic method [14], two particle distributions denote the two different fluids. Each fluid is assigned a 'color' (the use of the word 'color' is meant for identifying the fluid only) at all locations in the domain of interest. The model carries certain disadvantages which crucially underpin its applicability: (1) the re-coloring step is known to introduce lattice pinning and (2) the perturbation step has the side effect of introducing anisotropy and high spurious velocities at the interface. In Shan–Chen's (SC) model [15] adopted here, the multiple phases were simulated by introducing non-local interactions between particles at each lattice site. Hou et al. [16] in one of the earliest works on multiphase LBM compared the chromodynamic [14] and the pseudo-potential [15] models and showed that the Shan–Chen model was superior using a static bubble test which has since become a benchmark for conducting multiphase simulations using LBM. However, it was also found to have some shortcomings: velocity vectors were high at the interface; the model worked well for low density ratios. To counter this, a few models [17–20] were proposed. However, these models involve iterative procedures that are computationally expensive when the interface shape is rapidly evolving. In addition, the method in [17] has been shown to be lacking in Galilean invariance, which greatly prohibits its use in this study. Despite its shortcomings, the SC model is widely being used to simulate multiphase flows in a variety of recent studies because of its ease of implementation and isotropic nature of solutions [21–23].

Since the proposed work is to understand the droplet interactions at low density ratios, SC model has been used. The SC model incorporates non-local interactions among particles to simulate multiple component fluids. The interaction potential between components σ and $\bar{\sigma}$ is defined as

$$V(\mathbf{x},\mathbf{x}') = G_{\sigma\bar{\sigma}}(\mathbf{x},\mathbf{x}')\psi^{\sigma}(\mathbf{x})\psi^{\bar{\sigma}}(\mathbf{x}') \tag{7}$$

where $G_{\sigma\bar{\sigma}}(\mathbf{x},\mathbf{x}')$ is the Green's function. The quantity ψ^{σ} is the "effective mass". If only nearest neighbor interactions were considered, then

$$G_{\sigma\bar{\sigma}}(\mathbf{x},\mathbf{x}') = \begin{cases} 0; & |\mathbf{x}-\mathbf{x}'| > c \\ G_{\sigma\bar{\sigma}}; & |\mathbf{x}-\mathbf{x}'| = c \end{cases} \tag{8}$$

The magnitude of $G_{\sigma\bar{\sigma}}$ controls the strength of the interaction between components σ and $\bar{\sigma}$, while its sign determines whether the interaction is attractive or repulsive.

This form of the potential gives the net force due to surface tension-based interactions at each lattice site to be

$$\mathbf{F}_{int}^{\sigma}(\mathbf{x}) = -\psi^{\sigma}(\mathbf{x}) \sum_{\bar{\sigma}=1}^{S} G_{\sigma\bar{\sigma}} \sum_{a=0}^{b} \psi^{\bar{\sigma}}(\mathbf{x}+\mathbf{e}_a)\mathbf{e}_a \tag{9}$$

Similarly, at the solid–fluid interface, a force as proposed by [24] can be incorporated. This form of the interaction can be written as

$$\mathbf{F}_{wall}^{\sigma}(\mathbf{x}) = -\rho^{\sigma}(\mathbf{x}) \sum_{a=0}^{b} G_{w,\sigma}\rho^{\bar{\sigma}}(\mathbf{x}+\mathbf{e}_a)\mathbf{e}_a \tag{10}$$

where the interaction parameter $G_{w,\sigma}$ denotes the intensity of interaction from the wall and the sign (positive/negative) indicates whether the interaction is repulsive/attractive (non-wetting/wetting). For the D3Q19 lattice used in this work,

$$G_{w,\sigma}(\mathbf{x},\mathbf{x}') = \begin{cases} G_w; & |\mathbf{x}-\mathbf{x}'| = 1 \\ G_w/2; & |\mathbf{x}-\mathbf{x}'| = \sqrt{2} \\ 0; & \text{otherwise} \end{cases} \tag{11}$$

The external force is directed in the negative vertical direction. This external force can be introduced into the force equation using the expression [25]

$$\mathbf{F}_{ext}^{\sigma} = \rho^{\sigma}\mathbf{a}_{ext} = \rho^{\sigma}\mathbf{g}\left(1 - \frac{\langle\rho\rangle}{\rho}\right) \tag{12}$$

where ρ is the mixture number density at the node of interest and $\langle\rho\rangle$ is the average number density of the mixture in the entire domain. This choice ensures that the average value of the external force is zero in the periodic domain, and hence the mass-average velocity of the mixture is constant.

The total force on each component at each lattice site can thus be found by combining (9), (10), and (12). Thus

$$\mathbf{F}_{tot}^{\sigma} = \mathbf{F}_{int}^{\sigma} + \mathbf{F}_{wall}^{\sigma} + \mathbf{F}_{ext}^{\sigma} \tag{13}$$

Therefore, this change in momentum is applied at each lattice site in the equilibrium distribution function before the collision, as shown in [26]:

$$\rho^{\sigma}\mathbf{u}^{\sigma} = \rho^{\sigma}\mathbf{u} + \tau^{\sigma}\mathbf{F}_{tot}^{\sigma}(\mathbf{x}) \tag{14a}$$

where

$$\rho^{\sigma} = m^{\sigma}f^{\sigma}(\mathbf{x}) \tag{14b}$$

is the mass density of the σth component and

$$\mathbf{u} = \frac{\sum_{\sigma}^{S} m^{\sigma}\sum_a f_a^{\sigma}\mathbf{e}_a/\tau^{\sigma}}{\sum_{\sigma}^{S} m^{\sigma}\sum_a f_a^{\sigma}/\tau^{\sigma}} \tag{14c}$$

and

$$f^{\sigma}(\mathbf{x}) = \sum_a f_a^{\sigma} \tag{14d}$$

3. Results and discussion

The current modeling technique of LBM using what has been termed as the pseudo-potential method [15] was first validated for simulation of bubbly flows in fully periodic domains. The drag force was calculated and the bubble shape regimes were matched with the experimentally observed shapes [27].

Multiphase simulations of droplet impact on a wall were started by conducting static droplet tests to generate a good initial condition with one (or more) droplet in a channel in which the top and bottom boundaries are walls and the side boundaries are periodic. Changing the boundary condition criteria on the upper boundary of the domain to a free-slip layer from the no-slip condition did not yield significantly different results presented herein. The nearest neighbor SC model as explained in [28] has been used in which the next-nearest neighbor is also used in the force discretization, which results in isotropic solution and also reduces parasitic currents. Accordingly, Eq. (8) is modified to account for the nearest and second nearest neighbors as

$$G_{\sigma\bar{\sigma}}(\mathbf{x},\mathbf{x}') = \begin{cases} g; & |\mathbf{x}-\mathbf{x}'| = 1 \\ g/2; & |\mathbf{x}-\mathbf{x}'| = \sqrt{2} \\ 0; & \text{otherwise} \end{cases} \tag{15}$$

This leads to a non-ideal equation of state that is given by

$$p = c_S^2\rho + 3g\Psi^2(\rho) \tag{16}$$

where $c_S = 1/\sqrt{3}$ is the speed of sound. It should be noted here that if there is no interaction among the same kind of fluid, then the equation of state would reduce to the ideal gas equation of state given by $p = c_S^2\rho$. The 'effective mass' function, Ψ, is given by [15]

$$\Psi(\rho) = \rho_0[1 - \exp(-\rho/\rho_0)] \tag{17}$$

For the current equation of state, the value of the critical interaction strength is $g_{crit} = -\frac{2}{9\rho_0}$. Any value of the interaction strength below g_{crit} would result in phase separation of the liquid phase. In this study, the values of this fluid–fluid interaction parameter are selected in a way that a particular density ratio and a specific Weber number can be achieved. A low value of the interaction strength would result in a higher density ratio. In the simulation results described below, $\rho_0 = 10$. The computational domain is divided into $120 \times 120 \times 120$ lattice points which were tested to be adequate to resolve the thin films on the wall. The size of the domain was deemed large enough based on progressively increasing the size of the domain for the same initial droplet diameter and recording the spreading factor for the same Re and We.

Droplet impact and the dynamics depend on Weber number, We, and Reynolds number, Re. One other parameter that is very important in drop impact on dry surfaces is the spreading film diameter. This quantity is usually represented in terms of the spread factor given by the ratio of the diameter of the film and the diameter of the droplet, $\xi = d/D$. The fluid-interaction parameter was varied between −0.024 and −0.027, and the corresponding density ratio in the simulations ranged from 4 to 10. In addition, the fluid-interaction parameter controls the interfacial tension between the two fluids. The suspended droplet was equilibrated for 15,000 lattice timesteps, after which it was allowed to fall in the downward direction towards the solid surface. This was done to ensure that a steady liquid–vapor interface of approximately 3 lattice nodes was developed and did not change. This was also observed by recording the density of the liquid and vapor far away from the interface and monitoring the surface tension coefficient. The gravitation force was not present during the equilibration period. The time evolution of the spread factor is provided in Fig. 1 for a ratio of 6 at Re = 21.5 and We = 20.4. The time evolution can be divided into four phases, (a) the kinematic phase, (b) the spreading phase, (c) relaxation phase, and (d) equilibrium phase. It has been shown previously through experiments [5] that the film diameter increases as $\xi \propto \sqrt{t^*}$ in the kinematic phase. As the spreading phase begins, other parameters such as the diameter of the impacting droplet, the velocity, the surface tension and viscosity can start to influence the rate at which the lamella spreads. During the later stage of this phase, surface tension effects can play a prominent role in undermining the maximum spread the film can achieve. In the relaxation phase, the film diameter may begin to recede depending on the surface roughness and the impact velocity, before reaching the equilibrium phase where ξ reaches a constant. In the next few sections, the role of these physical properties and their influence on the spreading and breakup behavior of liquid droplets in a low density environment are discussed.

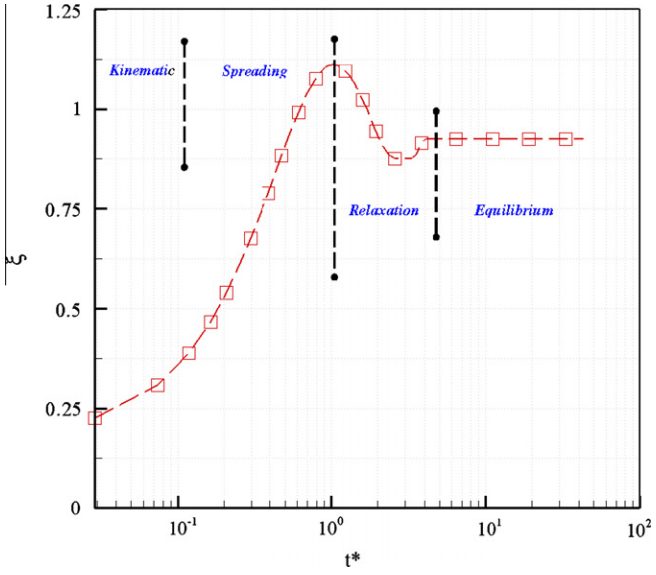

Fig. 1. Spreading behavior from the current LBM simulations showing the four phases of droplet impact dynamics at We = 20.4 and Re = 21.5 at a density ratio of 6.

3.1. Spreading of a liquid droplet

The spreading diameter was calculated based on the number of lattice points that are in contact with the heavier fluid at the wall. In the kinematic phase the contact line corresponds to the circumference of a horizontal cut through the drop moving with a downward velocity of V_0 [5]. Assuming that the diameter of the drop after the impact is still the same, a simple expression can be obtained in the kinematic phase ($t^* \ll 1$) for the spread factor as $\xi = d/D = 2t^{*1/2}$ where $t^* = tV_0/D$. This expression was validated for different We and Re using LBM as shown in Fig. 2. A curve fit

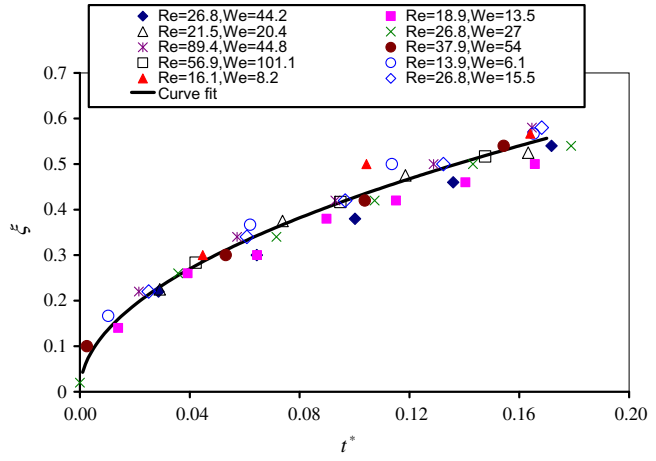

Fig. 2. Variation of the instantaneous spread factor with time in the initial phase of a three-dimensional drop impact on the dry solid surface. The solid line indicates the curve fit $d/D = 1.35t^{*0.5}$.

was generated to yield $d/D = 1.35t^{*0.5}$. A similar expression was also obtained in the experiments in [5] with a coefficient of 2.8. The static contact angles were fixed using the $G_{w\sigma}$ values. For studying the dependence of contact angle in the kinematic phase, the contact angle was varied between 60° and 120°. In the current simulation, it was also found that changing the wettability of the surface did not lead to different results in the kinematic phase of the spreading mechanism.

The kinematic phase is followed by the spreading phase in which the impact velocity, drop diameter and the surface tension determine the maximum spreading diameter. A comparison for the maximum spread factor from the 3D LBM simulations with experimental data of [6,29] is shown in Fig. 3. The experimental results of [6] show that the maximum spreading diameter is better correlated with the parameters, Reynolds number and Ohnesorge number. Ohnesorge number is given by $\mu/(\rho\sigma D)^{1/2} = \mathrm{We}^{1/2}/\mathrm{Re}$ which is dependent on only the fluid properties. Our numerical results are also compared with the correlation proposed in [6] (Fig. 3a), and with the analytical expression of [30] given as $\xi_{\max} = 0.5\mathrm{Re}^{0.25}$ which is applicable for $\mathrm{We} > 12$ and $\mathrm{Re}^{1/2} \ll \mathrm{We}$ (Fig. 3b). The simulation results from LBM match well with these studies.

For Oh = 0.194, droplet spreading on a dry solid surface is plotted in Fig. 4. The cross-sectional view of the three-dimensional spreading droplet is drawn through the center of the droplet. The corresponding plots of spread factor for Oh = 0.194 are given in Fig. 5. As the droplet impinges on the surface, it spreads until it is stretched to a maximum, beyond which the contact line recedes non-uniformly until the droplet comes to an equilibrium position. The droplet spreading process is quicker in the spreading phase ($t^* < 1$) in which the drop spreads due to an elongational flow after colliding with the surface. The droplet shapes are plotted at two times, one in the spreading phase for $t^* = 0.75$ and another in the relaxation phase at $t^* = 2.54$ for three different Weber numbers.

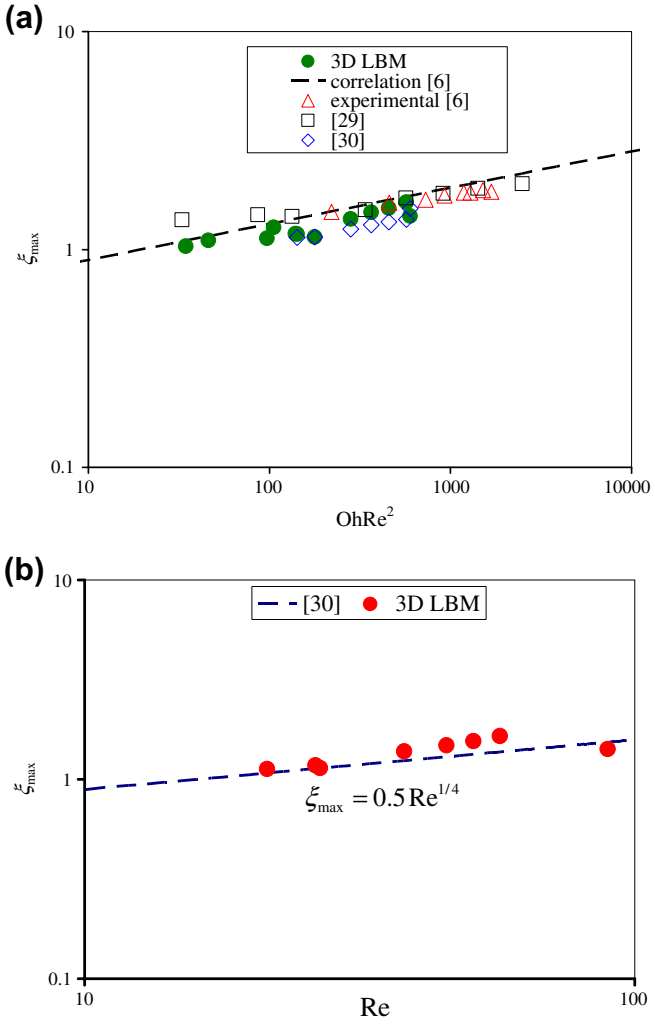

Fig. 3. Comparison with (a) experimental data points of [6,29], and the correlation of [6] and (b) analytical solution [30].

Fig. 4 shows the elongational flow at $t^* = 0.75$ as the droplet has entered into the spreading phase from the initial kinematic phase of the process. In this stage, the velocity of the droplet in the transverse (horizontal) direction drives it faster to an extremum. Beyond this stage, the relaxation phase of droplet spreading begins in which the droplet contact line recedes due to surface tension effects ($t^* = 2.54$), eventually leading to a steady state when the shape of the droplet does not change. The final shape looks like a torus beyond which there is no significant motion, and is very similar to what has been observed by [31], who report the experimental results of impact of spherical water drops traveling at moderate velocities. They found that these drops evolve to a staircase pyramidal shape, which eventually relaxes to a torus. The current study reproduces the numerical results of [31] including the torus shape but not the staircase pyramidal shape. The formation of a closed vortex near the interface of the two phases is also observed in Fig. 4. This vortex is the result of a drag on the lighter phase induced by the movement of the liquid film that spreads and recedes. As the droplet accelerates or decelerates on the surface, the strength of the vortex can similarly increase or decrease.

Comparing the droplet shapes in Fig. 4 with the spread factors in Fig. 5, for the same Ohnesorge number of 0.194, as the Weber number increases, the maximum spread factor increases. As seen in Fig. 2, $\xi \propto \sqrt{t^*}$ for all Weber numbers in the kinematic phase. As the Weber number increases, it takes longer for the droplets to reach the peak diameter. Similarly, simulations run at the same We and Oh (not plotted here) showed that as Reynolds number is increased, the droplet reaches its equilibrium shape at higher t^*. The longer time for a higher Re is due to lower viscous dissipation. Thus, for a given Ohnesorge number, the droplet spreading behavior is seen to be a strong function of the Weber number, which determines the maximum diameter of the spreading film, and the Reynolds number, which controls the time it takes for the droplet to reach the equilibrium shape. The equilibrium diameters of the droplets when they settle down tend to increase with increasing Weber number. For the lowest Weber number of 13.5, the droplet diameter does not exceed the original diameter in any of the phases. As the Weber number increases, it can be seen from Fig. 4 that the droplet takes a discoid form with a height much less than the original diameter at both $t^* = 0.75$ and 2.54.

The effect of Oh on the spread factor is plotted in Fig. 6 for an Oh range of 0.177–0.248 for different combinations of We and Re. The Ohnesorge number does not particularly control the peak of the spreading diameter. As seen in Fig. 5, for Oh = 0.177, the results suggest that the peak is controlled by the Weber number. What is interesting with these results, however, is that as the Ohnesorge number is decreased, for low Weber number, oscillations in the relaxation phase begin to appear. Another important parameter that emerges from Weber number and Reynolds number is the Capillary number, $\mathrm{Ca} = \mu U/\sigma = \mathrm{We}/\mathrm{Re}$, which is the ratio of the viscous to surface tension forces. In the seven cases shown in Figs. 5 and 6, in all except one Ca is greater than or about 1, and the oscillation in the relaxation phase is minimum.

As the Ohnesorge number is decreased further to 0.147 and 0.075 for the same Capillary number of $\mathrm{Ca} \sim 0.5$ (Fig. 7), the damping of these oscillations is reduced. Earlier experiments [32] have indicated that droplet spreading and breakup mechanism are a

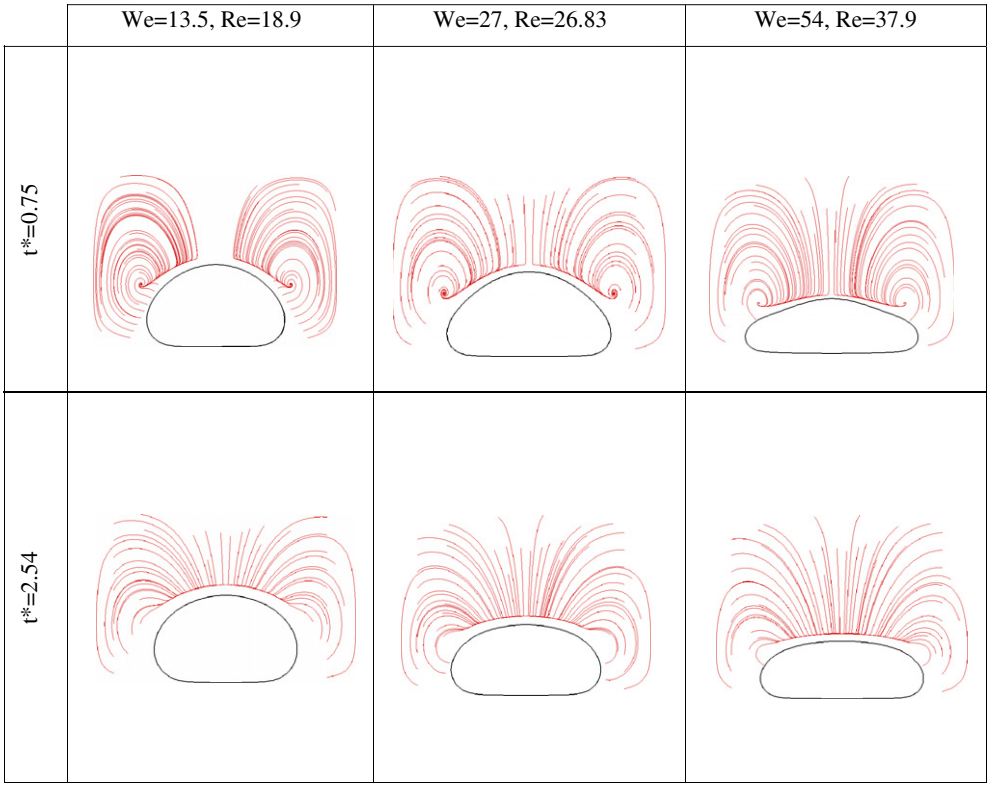

Fig. 4. Sequence of droplet falling on a wetting surface and subsequent spreading process for Oh = 0.194. Streamlines around the impinging droplet are shown in a truncated computational domain. The contours (shown in black) denote the interface.

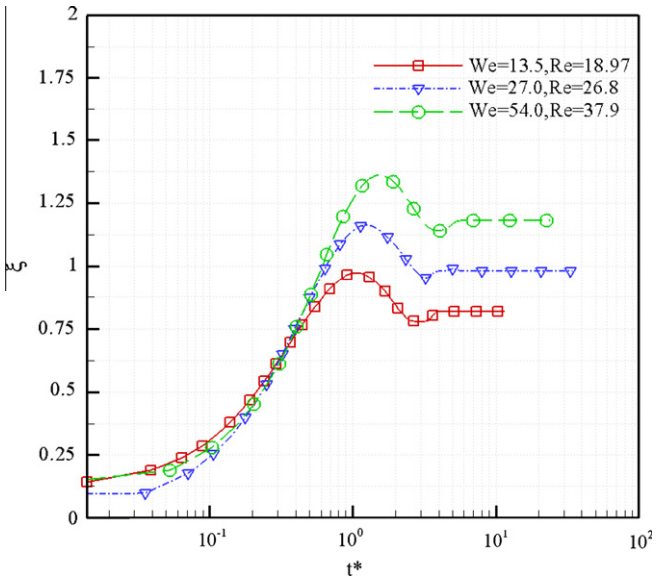

Fig. 5. Spread factor for the Oh = 0.194 cases.

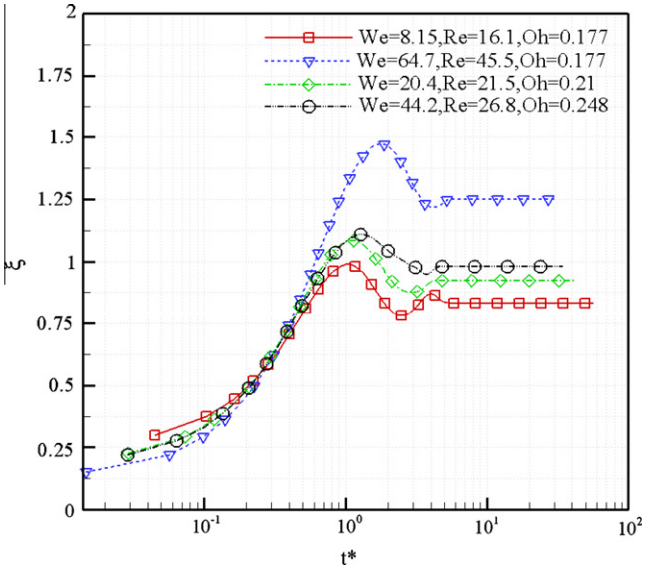

Fig. 6. Spread factor plotted as a function of the non-dimensional time for a range of We and Re.

strong function of the surrounding density (or pressure). In order to obtain the Weber numbers in these simulations, density ratio was slightly varied from 6 to 10. These damped oscillations are attributed to the drag experienced by the spreading film. At higher Weber number, the drag experienced by the receding film is higher, and the drag is proportional to the surrounding density. Thus, these three-dimensional simulations show that for Ca < 1 and Oh < 0.15, the oscillations in the spreading phase are prominent.

The current simulations are only capable of capturing droplet impact dynamics with large surface tension. This leads to a slower receding of the contact line, and hence longer relaxation phase. This is the reason why the present model is unable to capture the rebound of the liquid drop from the surface as also shown by [12,33].

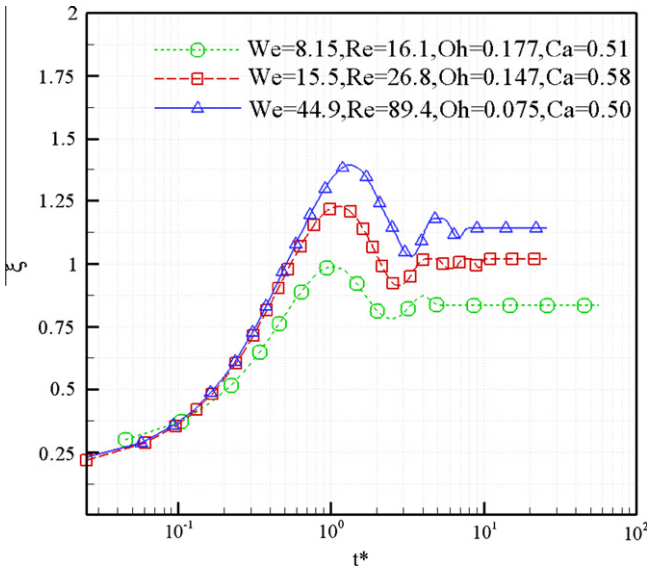

Fig. 7. Spread factor for Oh < 0.177 and Ca ~ 0.5.

3.2. Droplet breakup analysis

At slightly higher Weber and Reynolds numbers, an impinging droplet can breakup into smaller drops. The dependence of this breakup behavior although may depend on the above mentioned parameters, its dependence on the surface wettability and the manner of the dissipation of the impact kinetic energy is not well understood. By the principle of conservation of energy of the liquid drop before and after impact, we can write

$$E^i_{KE} + E^i_{PE} + E^i_{SE} = E^f_{KE} + E^f_{PE} + E^f_{SE} + E^f_D \tag{18}$$

where E^i_{KE}, E^i_{PE} and E^i_{SE} are the kinetic, potential and surface energies before the impact of the liquid drop with the solid, and E^f_{KE}, E^f_{PE}, E^f_{SE} and E^f_D are the kinetic, potential, surface and dissipation energies after the impact [34].

For a spherical drop falling on a solid surface, the kinetic energy of impact per unit length can be written as

$$E_{KE} = \frac{1}{2}\Delta\rho U^2\left(\frac{\pi}{6}D^3\right) \tag{19}$$

where $\Delta\rho = \rho_l - \rho_g$. If the drop spreads to a maximum diameter of D_{max} and a film thickness of h, then by conservation of mass

$$\frac{\pi}{6}D^3 = \frac{\pi}{4}D^2_{max}h \;\Rightarrow\; h = \frac{2}{3}\left(\frac{D}{d_{max}}\right)^2 D = \frac{2}{3}\frac{D}{\xi^2_{max}} \tag{20}$$

where ξ_{max} is the ratio of the maximum film diameter to the initial diameter of the drop.

The energy lost in dissipating the kinetic energy of the falling drop against viscosity has been shown to follow [35]

$$E_D \approx V\Phi t_e \tag{21a}$$

where Φ is the dissipation function given by

$$\Phi = \mu\left(\frac{\partial u_i}{\partial x_j} + \frac{\partial u_j}{\partial x_i}\right)\frac{\partial u_i}{\partial x_j} \;\Rightarrow\; \Phi \approx \mu\left(\frac{U}{h}\right)^2 \tag{21b}$$

and $t_e = \frac{D}{U}$ is the time taken by the droplet height to go from D to 0.

Thus, the dissipation energy is given by

$$E_D = \frac{3\pi}{8}\mu U\xi^4_{max}D^2 \tag{21c}$$

The surface energy is dependent on the surface tension. Before the impact, it is given by

$$E^i_{SE} = \pi D^2\sigma \tag{22}$$

When the spreading film has stretched to a maximum diameter given by d_{max}, the surface energy can be written as

$$E^f_{SE} = \frac{\pi}{4}d^2_{max}\sigma(1-\cos\theta) = \frac{\pi}{4}\xi^2_{max}D^2\sigma(1-\cos\theta) \tag{23}$$

The final surface energy is a function of the contact angle. In earlier studies, it has been found that the maximum spread factor has little dependence on the contact angles for Re > 10 flows. Thus, it is assumed that the final surface energy is not dependent on the contact angle, and by substitution of these expressions in Eq. (18), and on simplification, the energy equation can be reduced to

$$\frac{3(\xi^2_{max}-12)}{We} + \frac{9\xi^4_{max}}{2Re} = \frac{\Delta\rho}{\rho_l} \tag{24}$$

For large differences in density, the right hand side of Eq. (24) is 1.0. However, in the current study, $\Delta\rho/\rho_l$ can vary from 0.75 to 0.9.

At the instant when the spreading film diameter has reached a maximum, the interplay of the surface and kinetic energies can lead to a possible breakup of this liquid film into smaller daughter droplets. Eq. (24) can be regarded as a criterion for predicting spreading or breakup outcomes of an impacting droplet. For a situation when $\frac{\rho_l}{\Delta\rho}\left(\frac{3(\xi^2_{max}-12)}{We} + \frac{9\xi^4_{max}}{2Re}\right) > 1$, the spreading film will reach a maximum diameter without breaking up into daughter droplets, whereas when $\frac{\rho_l}{\Delta\rho}\left(\frac{3(\xi^2_{max}-12)}{We} + \frac{9\xi^4_{max}}{2Re}\right) < 1$, the spreading film will break into smaller drops when the maximum diameter has been reached.

For a water drop impinging a neutral surface and with air as the surrounding medium, i.e., $\Delta\rho/\rho_l = 1$ in a three-dimensional system, the demarcation line can be defined. From different experiments, the maximum spread factor at breakup has been found to be between 4 and 5 [1]. Using these values in Eq. (24), for the maximum spread factor at breakup, the analytical expression reduces to $12/We + 1152/Re = 1$ for $\xi_{max} = 4$ and $39/We + 2812/We = 1$ for $\xi_{max} = 5$. The map for all such outcomes is given in Fig. 8. The hatched portion between the curves may be considered the region where the droplet may or may not break after reaching the maximum spread factor. For low values of Re and We, i.e., on the left side of the region, the drop will never break. On the right side of this region, the drop will always break. The two limiting cases for the drop to break are given by (1) $Re \to \infty$ and hence We = 12–39, or (2) $We \to \infty$ and Re = 1152–2812. Hence, in 3D,

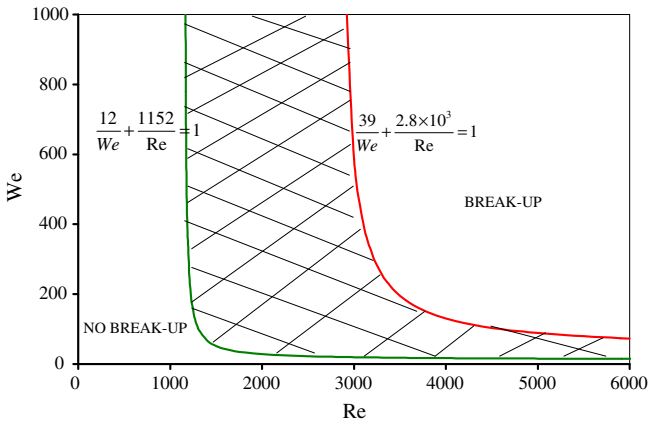

Fig. 8. The hyperbolic curve shown with the regimes of droplet impingement with and without breakup for a three-dimensional droplet impingement. The curve on the left indicates the breakup criterion for an assumed value for the maximum spread factor of 4. The right curve represents the maximum spread factor of 5.

for two fluids with a high-density ratio, an impinging water drop will definitely not break into smaller drops only if the condition 12/We + 1152/Re > 1 is satisfied. The We = 12 limit is well known from the literature. An extensive analysis for a range of We and Re at different density ratios is not possible for a 3D droplet breakup due to the instability that is propagated for low viscosity solutions using the SC model. This is because the Shan–Chen model with multiphase flows was only found to be stable with a relaxation time, τ, of 1. Since the kinematic viscosity of the fluid depends on the relaxation time as $\nu = (\tau - 0.5)c_s^2\Delta t$, this restricts the maximum Reynolds number that can be achieved.

4. Conclusions

In the present study, the lattice Boltzmann method has been used to perform three-dimensional simulations of droplet impact dynamics using a model that allows two-phase interactions. This model incorporates fluid–fluid and fluid–solid interactions. The strength of the fluid–fluid interaction is used to vary the surface tension force and the density ratio in the current simulations, whereas the strength of the fluid–solid interaction alters the wetting nature of the fluid. The density ratio was varied between 3 and 10. The fluid–fluid interaction parameter has been used to attain a constant density ratio and the corresponding interfacial tension coefficient.

The model was extended to study the spreading behavior of a single drop colliding with a solid dry surface for a range of Weber (5 < We < 100) and Reynolds (10 < Re < 100) number. The current LBM model is shown to be capable of capturing the four phases of droplet spreading on a solid surface, namely (a) kinematic phase, (b) spreading phase, (c) relaxation phase, and (d) equilibrium phase. In the kinematic phase, the wettability had no influence on the spreading diameter, which was found to obey the relationship, $d/D = 1.35t^{*0.5}$. In the spreading phase, it is found that the spread factor is higher for high inertia impacts, or high Weber number. The results are found to match well with existing experimental results [6,29] and with the analytical expression of [30] given as $\xi_{max} = 0.5\mathrm{Re}^{0.25}$ which is valid for We > 12 and $\mathrm{Re}^{1/2} \ll \mathrm{We}$.

For a given Ohnesorge number, the droplet spreading behavior is seen to be a strong function of the Weber number, which determines the maximum diameter of the spreading film, and the Reynolds number, which controls the time it takes for the droplet to reach the equilibrium shape. At Oh < 0.15 and Capillary number, Ca < 1.0, the relaxation phase is marked by the presence of strong oscillations in the spreading diameter. There is less damping of the droplet spreading and contracting for Re > 60, which may be attributed to (a) a lower drag when the surrounding fluid has a lower density, and (b) a slower viscous dissipation of the receding drop when the surrounding liquid has a lower viscosity, both of which lead to longer fluctuations in the spreading drop. Criteria for a spherical droplet breakup have been developed, which depend on Re and We. These criteria for 3D are provided without results since droplet breakup occurs at higher Re and We, which cannot be handled by the current model.

The Shan–Chen model adopted in this work suffers from some limitations. In particular, (a) velocity vectors were high at the interface, and (b) the model works well for low density ratios only (<10). To reduce the parasitic currents at the interface, the second-neighbor interactions were incorporated. Future work is directed towards the droplet breakup mechanism in three-dimensions using a model that can simulate high Reynolds and Weber numbers. Also under investigation are the effect of high-density ratio fluids and the study of the splashing behavior of drops falling onto wet surfaces.

References

[1] Yarin AL. Drop impact dynamics: splashing, spreading, receding, bouncing... Ann Rev Fluid Mech 2006;38:159.
[2] Wachters LHJ, Westerling NAJ. The heat transfer from a hot wall to impinging water drops in the spheroidal state. Chem Eng Sci 1966;21:1047.
[3] Stow CD, Hadfield MG. An experimental investigation of fluid flow resulting from the impact of a water drop with an unyielding dry surface. Proc Roy Soc Lond A 1981;373:419.
[4] Yarin AL, Weiss DA. Impact of drops on solid surfaces: self-similar capillary waves, and splashing as a new type of kinematic discontinuity. J Fluid Mech 1995;283:141.
[5] Rioboo R, Marengo M, Tropea C. Time evolution of liquid drop impact onto solid, dry surfaces. Exp Fluids 2002;33:112.
[6] Scheller BL, Bousfield DW. Newtonian drop impact with a solid surface. AIChE J 1995;41:1357.
[7] Morton D, Rudman M, Jong-Leng L. An investigation of the flow regimes resulting from splashing drops. Phys Fluids 2000;12:747.
[8] Josserand C, Zaleski S. Droplet splashing on a thin liquid film. Phys Fluids 2003;15:1650.
[9] Mukherjee S, Abraham J. Lattice Boltzmann simulations of two-phase flow with high density ratio in axially symmetric geometry. Phys Rev E 2007;75:026701.
[10] Mukherjee S, Abraham J. Crown behavior in drop impact on wet walls. Phys Fluids 2007;19:052103.
[11] Lee T, Lin CL. A stable discretization of the lattice Boltzmann equation for simulation of incompressible two-phase flows at high density ratio. J Comput Phys 2005;206:16.
[12] Mukherjee S, Abraham J. Investigations of drop impact on dry walls with a lattice-Boltzmann model. J Colloid Interface Sci 2007;312:341.
[13] Noble DR, Chen S, Georgiadis JG, Buckius RO. A consistent hydrodynamic boundary condition for the lattice Boltzmann method. Phys Fluids 1995;7:203.
[14] Rothman D, Keller J. Immiscible cellular-automaton fluids. J Stat Phys 1988;52:1119.
[15] Shan X, Chen H. Lattice Boltzmann model for simulating flows with multiple phases and components. Phys Rev E 1993;47:1815.
[16] Hou S, Shan X, Zou Q, Doolen GD, Soll WE. Evaluation of two lattice Boltzmann models for multiphase flows. J Comput Phys 1997;138:695.
[17] Swift M, Osborne W, Yeomans J. Lattice Boltzmann simulation of nonideal fluids. Phys Rev Lett 1995;75:830.
[18] Inamuro T, Tajima S, Ogino F. Lattice Boltzmann simulation of droplet collision dynamics. Int J Heat Mass Transfer 2004;47:4649.
[19] Kurtoglo IO, Lin CL. Lattice Boltzmann simulation of bubble dynamics. Numer Heat Trans B 2006;50:333.
[20] He X, Chen S, Zhang R. A lattice Boltzmann scheme for incompressible multiphase flow and its application in simulation of Rayleigh–Taylor instability. J Comput Phys 1999;152:642.
[21] Kang Q, Zhang D, Chen S. Displacement of a two-dimensional immiscible droplet in a channel. Phys Fluids 2002;14:3203.
[22] Kang Q, Zhang D, Chen S. Displacement of a three-dimensional immiscible droplet in a duct. J Fluid Mech 2005;545:41.
[23] Huang H, Thorne DT, Schaap MG, Sukop MC. Proposed approximation for contact angles in Shan-and-Chen-type multicomponent multiphase lattice Boltzmann models. Phys Rev E 2007;76:066701.
[24] Martys NS, Chen H. Simulation of multicomponent fluids in complex three-dimensional geometries by the lattice Boltzmann method. Phys Rev E 1996;53:743.
[25] Sankaranarayanan K, Shan X, Kevrekidis IG, Sundaresan S. Analysis of drag and virtual mass forces in bubbly suspensions using an implicit formulation of the lattice Boltzmann method. J Fluid Mech 2002;452:61.
[26] Buick JM, Greated CA. Gravity in a lattice Boltzmann model. Phys Rev E 2000;61:5307.
[27] Gupta A, Kumar R. Lattice Boltzmann simulation to study multiple bubble dynamics. Int J Heat Mass Transfer 2008;51:5192.
[28] Yuan P, Schaefer L. Equations of state in a lattice Boltzmann model. Phys Fluids 2006;18:042101.
[29] Asai A, Makoto S, Hirasawa S, Okazaki T. Impact of an ink drop on paper. J Imaging Sci Technol 1993;37:205.
[30] Pasandideh-Fard M, Qiao YM, Chandra S, Mostaghimi J. Capillary effects during droplet impact on a solid surface. Phys Fluids 1996;8:650.
[31] Renardy Y, Popinet S, Duchemin L, Renardy M, Zaleski S, Josserand C, et al. Pyramidal and toroidal water drops after impact on a solid surface. J Fluid Mech 2003;484:69.
[32] Xu L, Zhang WW, Nagel SR. Drop splashing on a dry smooth surface. Phys Rev Lett 2005;94:184505.
[33] Kim HY, Chun JH. The recoiling of liquid droplets upon collision with solid surfaces. Phys Fluids 2001;13:643.
[34] Mundo C, Sommerfeld M, Tropea C. Droplet-wall collisions: experimental studies of the deformation and breakup process. Int J Multiphase Flow 1995;21:151–73.
[35] Chandra S, Avedisian CT. On the collision of a droplet with a solid surface. Proc Roy Soc Lond A 1991;432:13.